Full length article

A novel methodology for investigating the through-thickness molten pool shape during remote laser beam welding

Venkat Vivek Pamarthi [a,*], Tianzhu Sun [a,*], Abhishek Das [b], Pasquale Franciosa [a]

[a] Warwick Manufacturing Group, University of Warwick, Coventry, United Kingdom CV4 7AL
[b] Department of Mechanical Engineering, Indian Institute of Technology Delhi, New Delhi, India 110016

ABSTRACT

Molten pool shape can retrieve information on thermal gradients and solidification rates which provide substantial process signatures on cracking and weld quality. However, monitoring the molten pool shape remains a challenging task due to the complex nature of the laser welding process. The current study employs a novel monitoring methodology to examine the role of through-thickness molten pool shape in solidification cracking in partially penetrated welds. A Coherent ARM (Adjustable Ring mode) fibre laser, featuring independent control of the core and ring beam with the ratio of respective beam power specified by power ratio, was employed to study different molten pool shapes. Experimental investigations further include welding of aluminium alloy and quartz glass in butt configuration with a high-speed imaging system facing the longitudinal cross-section of the weld. The molten pool shape was evaluated using the developed image processing algorithm and the curvature analysis. Furthermore, ad-hoc Digital Image Correlation (DIC) was used to examine the thermal strain development in the through-thickness direction. Results showed that the proposed methodology could provide an accurate detection of the through-thickness molten pool shape with an improved accuracy of 94.3 % compared to the advanced prior models available in the literature, with an accuracy of 30.23 % and 42.5 %. It also revealed a tail-like feature in the molten pool's rear end, which influences the crystallisation paths and facilitates premature solidification, leading to greater tensile strains during solidification. The increments in power ratio from 0.36 to 1.5 reduced the tail-like feature and reduced the shrinkage strains in the fusion zone.

1. Introduction

In recent years, the rise of the electric vehicle (EV) industry has fuelled the use of lightweight materials. Aluminium, particularly 6xxx series alloys, is the popular choice for lightweight EVs due to their strength-to-weight ratio [1]. Remote laser welding (RLW) is regarded as a crucial choice for welding aluminium alloys due to its ability to produce high-quality welds with higher welding speeds, flexibility and minimal distortion making it optimal for joining aluminium alloys [2]. Despite the advantages of RLW, it also presents challenges, specifically in terms of crack sensitivity. Solidification cracking, a common defect that evaluates the weldability of materials, is more prominent in aluminium alloys. It primarily stems from the existence of a large mushy zone, the size of which is related to the molten pool morphology [3]. As the molten pool solidifies, the solidification crack initiates at a temperature above the solidus and propagates through the liquid molten metal trapped between grain boundaries [4]. Therefore, the crack

sensitivity is affected by factors such as thermal gradients, cooling rates, and material flow, each of which inherently influenced by the molten pool shape during welding [5]. Further, the morphology of the molten pool adjacent to the keyhole provides important information of the quality of the weld and the occurrence of cracking [6]. This dependency of molten pool behaviour on the weld quality was demonstrated by a few researchers, mainly understanding different molten pool shapes, from elliptical to teardrop shape, distinctly influence the grain orientation and cracking in the top region [7,8]. More recent studies on the numerical simulations of the molten pool shape, observed that the narrowing of the pool shapes increased the local solidification sequence causing an increase in crack susceptibility [9]. However, a precise understanding of the correlation between real-time welding process and the occurrence of cracking still remains challenging.

Different in-situ sensors have been adopted in order to monitor the spatial morphology and dynamics of the molten pool and its effect on weld defects [10]. For instance, pyrometers and thermal IR camera are

* Corresponding authors.
E-mail addresses: venkat-vivek.pamarthi@warwick.ac.uk (V.V. Pamarthi), tianzhu.sun@warwick.ac.uk (T. Sun).

employed to retrieve the molten pool temperature, although they cannot provide three dimensional spatially distributed information [11,12]. On the other hand, recent researchers employed high speed imaging coupled with different image processing methods to predict the top molten pool shape. One study observed the effect of top molten shape oscillations to predict the penetration depth [13]. Furthermore, another study has adapted a series of frame subtraction and image morphological operations to predict the top surface molten pool shape and identified its effect on porosity and weld quality from the top surface [14–16]. It should be noted that these methodologies only provide an approximate interpretation of the edges of top molten pool and may misinterpret the true form of the molten region, especially, when considering the dynamic movement of the liquid and the complex texture of the images of welding. Additionally, despite the use of geometrical parameters for describing the shape of the molten pool on the top surface and evaluating weld quality, a complete three-dimensional detection to study the spatial weld quality is still unavailable. Furthermore, recent image processing problems focuses on using convolutional neural networks (CNN) to detect the weld pool morphology and to classify the weld defects [17]. These methods, although potent, require a large and diverse set of labelled data which is particularly challenging to produce in this context of welding. Therefore, due to these considerations, studies have opted against deploying of CNN in welding scenario analysis. Recently, the in-situ observation of

the keyhole morphology with high-speed cameras and X-ray sources was used to study its impact on cracking behaviour [18–20]. These observations phenomenologically explained that cracks produced from the small pores generated from the keyhole and exposed the impact of keyhole bulge on cracking. However, despite the potential benefits, conducting a comprehensive investigation using synchrotron X-ray imaging presents challenges due to the interaction of X-rays within the laser welding setup [21]. This interaction may lead to distorted data, differentiating the molten liquid from the solidified metal. Additionally, the relatively low thickness of the sheets used for welding, which is necessary to allow the X-rays to pass through, may not accurately represent real-world welding conditions. More recent studies introduced the use of a quartz glass plate for the in-situ observation of keyhole morphology, and this approach is assumed to be closely aligned with the realistic scenario [22–24]. These studies have observed the comparative deviations of molten pool and keyhole during vacuum welding conditions. However, these observations primarily focus on understanding the keyhole morphology and the effect of keyhole bulging on weld quality. The precise through-thickness shape of the molten pool and its consequential effect on solidification cracking has not been studied.

The main aim of this study is to present a novel in-situ monitoring methodology and elucidate the influence of through-thickness molten pool shape on the formation of solidification cracks during laser welding. The experimental investigation utilises a glass-aluminium butt weld
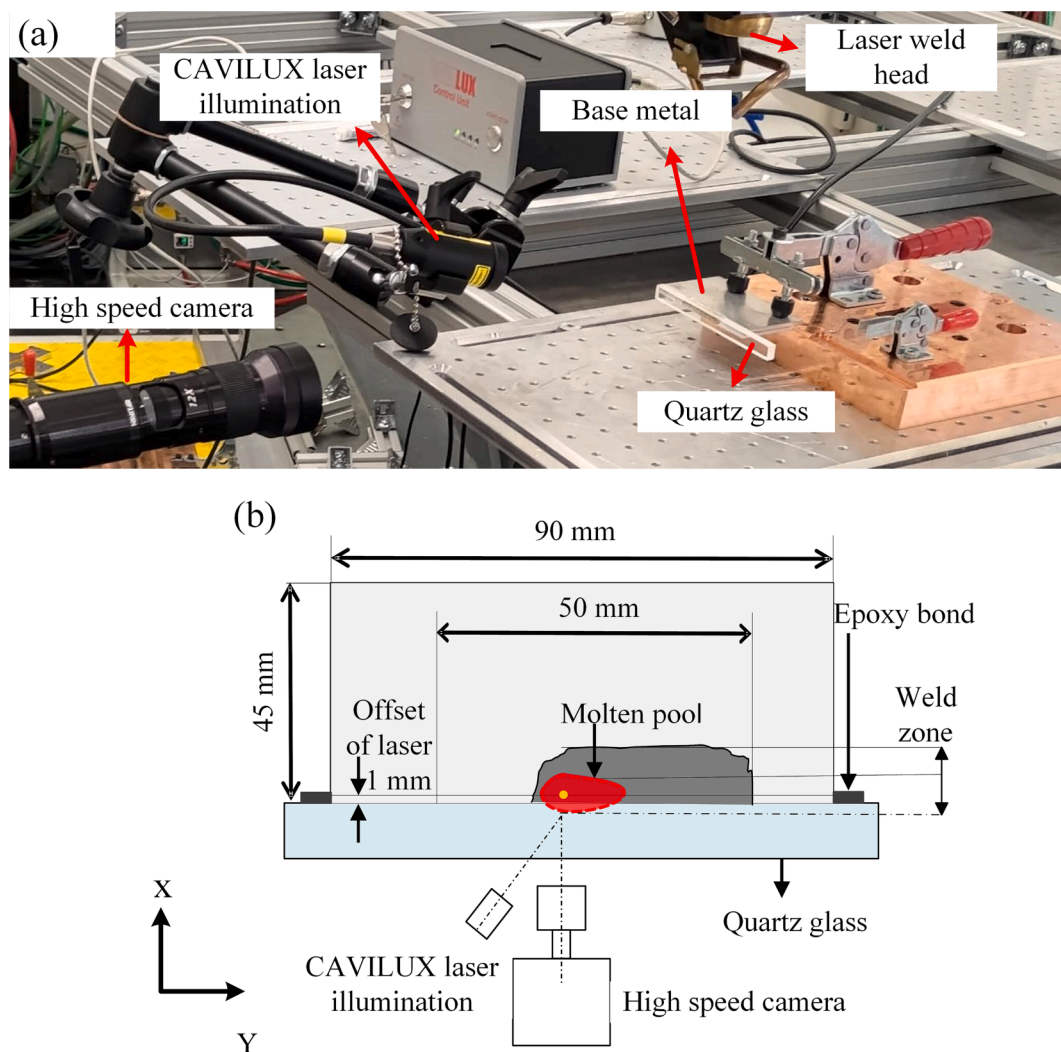

Fig. 1. Schematic representation of the (a) experimental setup, (b) with specimen geometry and the visualisation of the molten pool with a field of view of 25 x 15 mm^2.

experiment and a monitoring system using a high-speed camera in the thickness direction of the welding process. Later, a novel image processing algorithm was developed and implemented to detect the through-thickness molten pool shape. Additionally, it investigates the correlation between the curvature of the through-thickness molten pool shape and crystallisation paths of the growing dendrites.

2. Materials and experimental procedures

For the current study, 6005-T6 aluminium sheets with a thickness of 3 mm were employed. The sheets were machined into 90 mm (length) by 45 mm (width) and cleaned thoroughly with acetone to remove contaminations prior to welding. An overlap joint configuration was utilised, where the seam was stitched using an Duralco epoxy bond on both sides to a quartz glass in a butt configuration, as shown in Fig. 1. The quartz glass Spectrosil 2000 from Robson Scientific, UK, offers 98 % transparency at a wavelength of 1080 nm and has dimensions of 100 mm in length), 10 mm in width, and 10 mm in thickness, as illustrated in Fig. 1(b). Further, the chemical composition of the materials is given in Table 1. Given the unique properties of the quartz glass, such as low thermal conductivity, thermal expansion coefficient and high melting temperature, the quartz-aluminium interface can be regarded as the plane of symmetry, which allows a closer approximation to the real welding scenarios [22]. The centre of the focussed laser spot was on the aluminium base metal during welding and was adjusted with an offset of 1 mm from the intersection of the quartz-aluminium interface as shown in Fig. 1 (b) which determines distance from the centre of the weld to the field of view. This offset value is optimised to ensure the molten pool is clearly visualised and meanwhile to avoid the clouding of the glass due to violent expulsion of the molten pool. A FASTCAM Nova high-speed imaging system equipped with a narrow band pass filter and CAVILUX laser illumination was employed to collect the longitudinal cross-sectional images (y-z plane) of the molten pool at 15,000 fps, resolution of 896 x 512 pixels and an exposure time of 30 microseconds.

A 10 KW ARM fibre laser source (Coherent - Highlight FL10000-ARM) was employed and delivered by SCANSONIC ALO4-O remote laser weld head with a collimating length of 158 mm and focussing length of 176 mm. The ARM laser is comprised of ring and core beams, each independently rated at 5 kW. The beam diameter at the focused plane is 0.11 mm for the core and 0.32 mm for the ring beam. During the welding process, the weld head was intentionally tilted at negative 10° with respect to the X–axis, as shown in Fig. 1, to reduce the potential risk of melting the quartz glass and preserving its transparency. Table 2 presents the welding parameters employed in this study. For the purpose of ensuring reliable observations, each parameter was replicated three times in the study. Further, Finite Element-based Digital Image Correlation (FE-DIC) adopted from our previous study [27,28] was used to investigate the thermal strains developed during laser welding. Following the welding process, the samples were sectioned normal to the welding direction using Buehler AbrasiMet M abrasive cutter and metallographically prepared to a 0.06 μm surface finish using Buehler AutoMet 300 Pro polisher and were observed using Keyence optical microscope. Electron Back Scattered (EBSD) mapping was conducted using the JEOL-7800F scanning electron microscope, operating at 20 kV with a step size of 3 μm and the acquired data was processing using the

Table 1
Chemical composition (in wt. %) of the studied materials [25,26].

AA 6005 -T6 alloy								
Mn	Mg	Si	Fe	Mg + Cr	Cu	Zn	Others	Al
0.5	0.4	0.5	0.35	0.12	0.1	0.1	0.05	Bal
Spectrosil 2000 quartz glass								
Al	Ca	Fe	Cu	K		Na	Mg	Others	SiO$_2$
0.01	0.015	0.005	0.003	0.01		0.01	0.005	0.01	Bal

Table 2
Matrix of ARM laser welding process parameters.

Total Laser power (W)	Power of core (W)	Power of ring (W)	Power ratio (r = P_c/ P_r)	Focal position (mm)	Welding speed (mm/s)
4000	1100	2900	0.36	0	50
	2000	2000	1.00		
	2400	1600	1.50		

Aztec acquisition software.

3. Determination of molten pool shape

With the high-speed vision systems outlined in our study, a substantial number of images detailing the molten pool shape with a frame rate of 15,000 fps and at a resolution of 896x512 were captured. The raw image data were subsequently processed to elucidate the characteristics of the molten pool.

3.1. Methodology

Fig. 2 summarises the methodology employed in this study for determining molten pool morphology. The collected raw images of the molten pool are processed using Coarse-to-fine Lucas-Kanade (CF–LK) algorithm, which determines the changes in the pixel intensity between two successive images to detect the alterations in the molten pool shape via movements in the molten liquid across consecutive frames [29]. Further, a series of image morphological operations were employed to segment the accurate molten pool shape. The key advantage of the developed algorithm is its capacity to extract curvatures of the molten pool shape which changes in-process with time and between welds with various welding parameters. The processed images were then used for analysing the morphological features of the molten pool, i.e., curvature and irregular bend of the contour, and to develop the correlation between the molten pool morphology and through-thickness crack propagation. The crack propagation path was characterised by the path of growing dendrites in this study, based on the assumption that the preferred grain growth direction aligns with the normal of the molten pool curve [30] and primarily occurs along the direction of higher thermal gradients [3]. A detailed description of each step is introduced below:

3.1.1. Molten pool tracking

The modified Lucas-Kanade algorithm [31] was employed to estimate the apparent motion of the molten pool projected in the high-speed images. It determines the two-dimensional displacement field by evaluating the changes in the position of brightness patterns between successive images [32]. The LK-method operates on the assumption of brightness constancy between two successive time frames of an object in the image and is expressed in Eq. (1),

$$I(X, t) = I(X + u, t + dt) \tag{1}$$

where, X is the coordinates (x, y) and I is the intensities of the pixel from position (X, t) to (X + u, t + dt) for successive images and u is the displacement in x and y directions. In the LK method, as described by Eq. (1), the template representing a small region of the initial image is correlated with the corresponding region termed as target in the consecutive moving image. This involves considering the intensities I (X, t) and I (X + u, t + dt) as the template from the frame at t and the target at the frame t + dt as depicted in Fig. 3. By employing this assumption, the template was mapped to the target by a displacement vector u = [u, v] ^{T} at each Interrogation window (IW): $(IW): I(X, t) \rightarrow I(X + u, t + dt)$, $\forall X \in IW$[29]. The interrogation window is the small region of the image that was analysed by the algorithm to compute the local motion, as
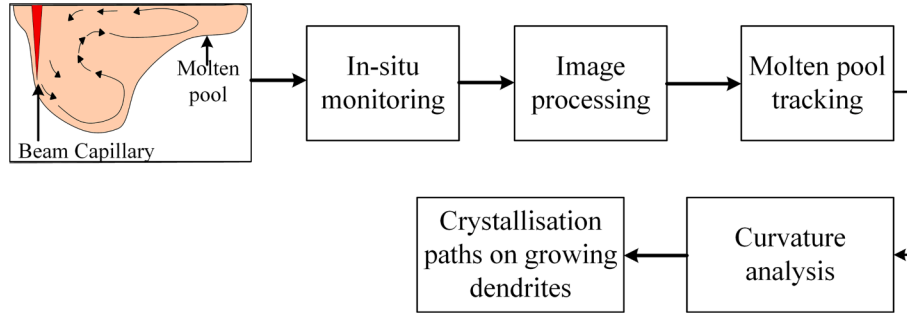
Fig. 2. Block diagram showing methodological approach developed in this study.
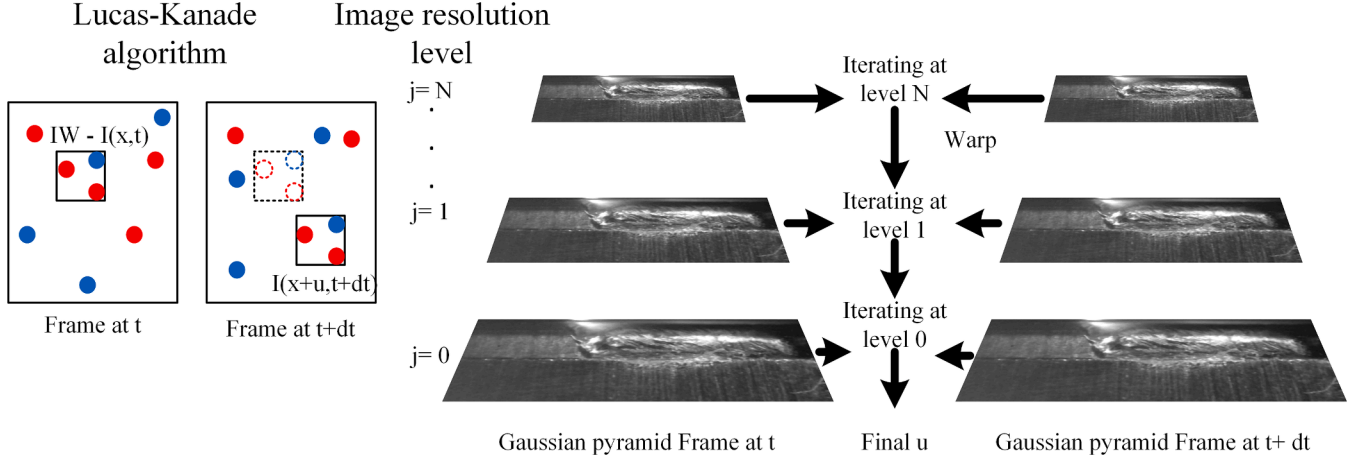

Fig. 3. Schematic illustration of the Coarse to fine Lucas-Kanade algorithm with the iteration steps at each level of resolution [29].

shown in Fig. 3. Later, the LK-method uses a minimisation of the Sum of Square Differences (SSD) integrated over IW to measure the correctness of the mapping and was optimised using the Gaussian-Newton (GN) descent approximation [29] as shown in Eq. (2).

$$\min_{u} \sum_{IW} [I(X, t) - I(X + u(X_c), t + dt)]^2 \qquad (2)$$

In Eq.2, the displacement vector u of IW was assigned to the local displacement at X_c, and the centroid pixel of IW. It should be noted that as the assumptions of brightness invariance and the regional uniformity of velocities are made in the LK method, substantial errors may occur in the case of distinctive motion of the molten pool. Therefore, a pyramidal approach termed as Coarse to fine Lucas-Kanade (CF-LK) algorithm was implemented to modify the resolution of the images [33]. The core idea of the CF-LK algorithm is to down sample the image pair (I^t, I^{t+dt}) successively to generate a pair of image pyramids $\left(I_j^t, I_j^{t+dt}\right)$, with j = 1,…N as shown in Fig. 3 with the N representing the reduction of resolution by 2^N [34]. Then the minimisation of SSD of the non-linear optimisation problem was translated with u_0 being the initial guess of the displacement u, and Δu is the incremental update of the guess with each layer of the pyramid: $u_0 + \Delta u_0 \to u$ by further using the Taylor series expansion of equation 1.2 is as follows,

$$\min_{u} \sum_{IW} [I_j^t(X) - I_j^{t+dt}(X + u_0) - \nabla I_j^{t+dt}(X + u_0)^T \Delta u]^2, \text{ where } j = 1,.....N \qquad (3)$$

where $\nabla I = [\partial I/\partial x, \partial I/\partial y]^T$ is the spatial gradient of I and the time stamp was moved to the subscript for simplification. The image pyramid was first built by reducing the resolution of images with the total level of refinement optimised to four (N = 4). Thereby, from Eq. (3), an

optimised interrogation window (IW) size of 9x9 pixels was used to estimate the velocities at coarser level and then refined at each level. Furthermore, warping was used to adjust the image at the finer level based on the flow velocities at coarser level as an initial guess [35]. By denoting the velocities of flow at previous level as (u', v') and the original image coordinates as (x, y), the warped image coordinates (x', y') is represented by:

$$(x', y') = (x + u', y + v') \qquad (4)$$

In this work, the proposed algorithm has been employed to derive the velocity fields in the moving molten pool as shown in Fig. 4 (a) and (b).

3.1.2. Removing outliers using DB-scan and image morphological operations

Further, the Density-based Spatial Clustering of application with noise (DBSCAN) algorithm was used to segment the processed images from the previous step specifically to isolate the large cluster of arbitrary shapes, presumably representing the molten pool shape. This algorithm involves the following steps: (i) Identify all non-zero velocity points from the images processed by the CF-LK method, as shown in Fig. 4 (c), which represent the movement in the raw image and the points of interest, that make up the molten pool shape. (ii) the identified velocity points were then clustered using the DBSCAN algorithm where a cluster is defined in a set of points that are either density-near or density-connected from another point, as depicted in Fig. 4 (d) [36]. After clustering, the identified label of the cluster with the maximum points was assumed to be the molten pool region, with the largest cluster set to one, effectively isolating the region of interest in Fig. 4 (e). This operation ensured to remove the random outliers which include random noise that do not represent the actual molten pool shape, such as those caused by spattering and plasma during welding. (iii) Morphological
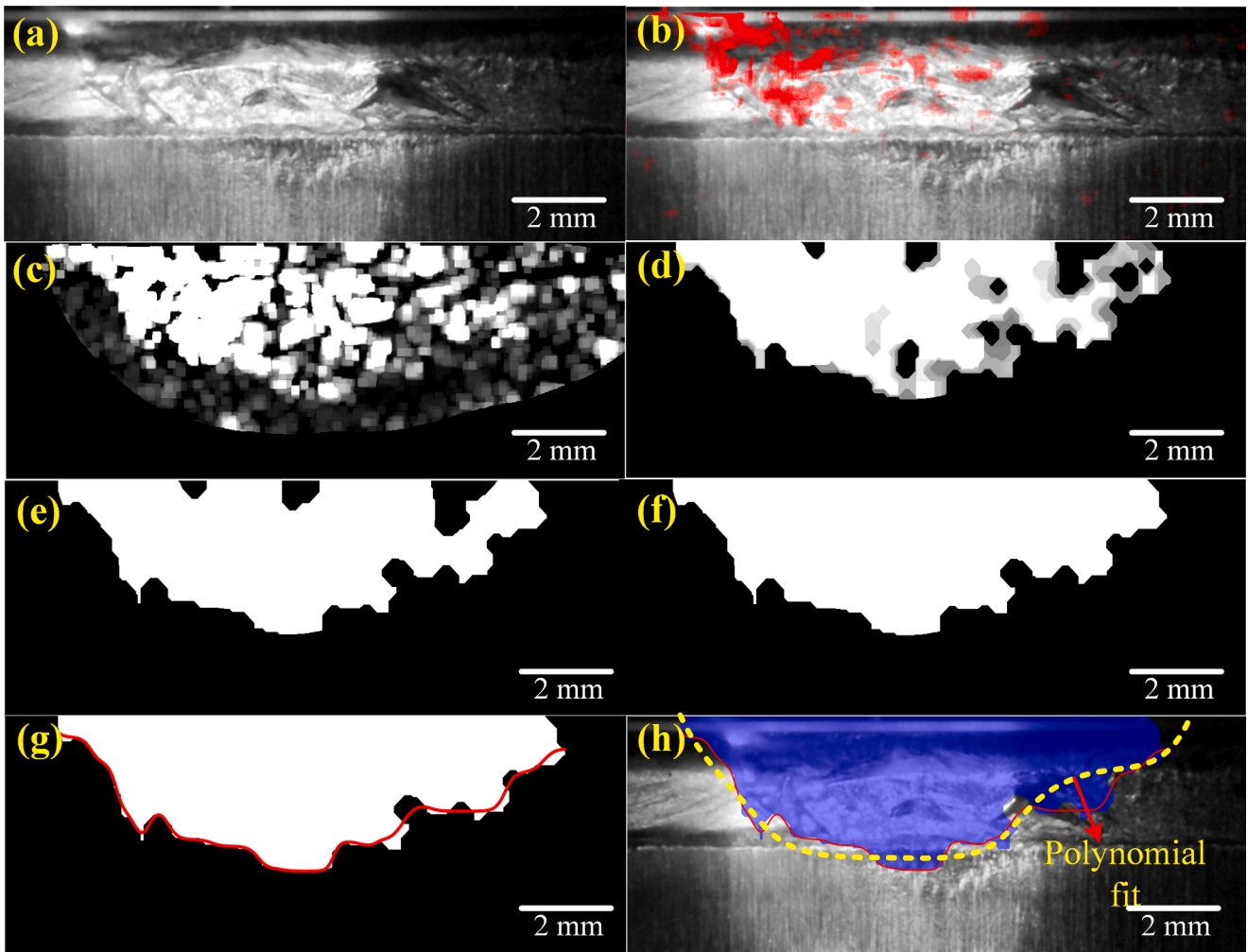
Fig. 4. Steps of the image processing algorithm developed (a) raw image, (b) velocity field from CF-LK algorithm, (c) velocity fields with a threshold without background, (d) Segmentation using the DB scan clustering, (e) Threshold to binary image and dilation, (f) Filling the holes, (g) fitting the boundary and (h) Overlaying on the original raw image.
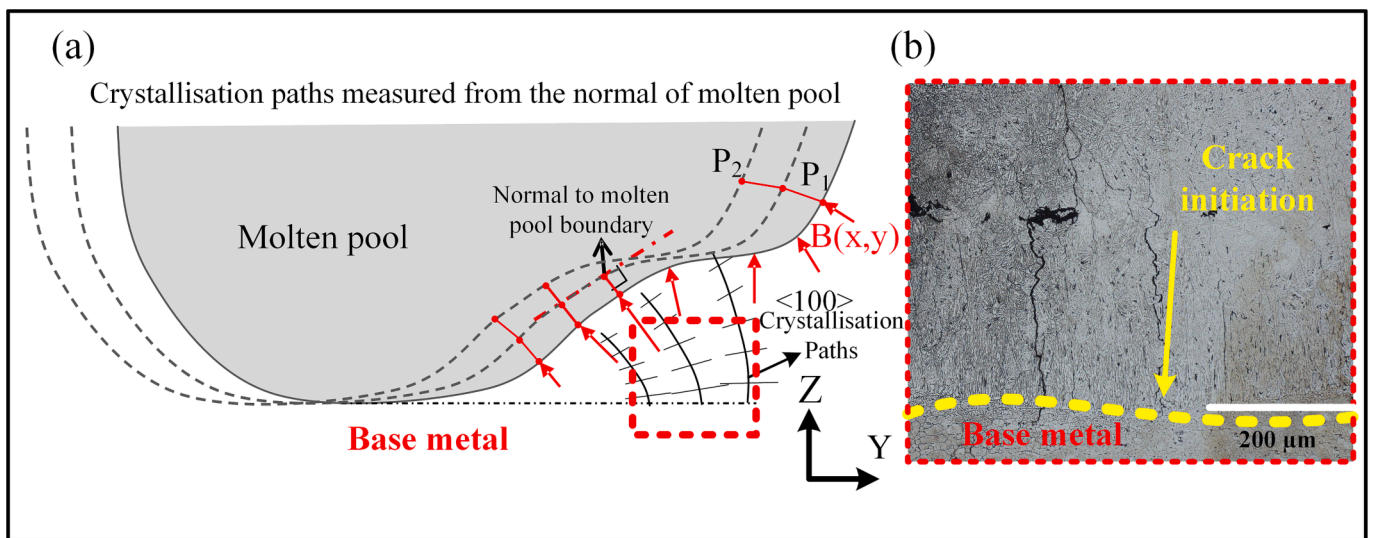

Fig. 5. Schematic of the predicted probable crystallisation paths inferred from the growth of grains along the maximum thermal gradient direction from Kou. et al. [30].

operations, e.g., erosion and dilation, were performed to connect and smoothen the edges, as shown in Fig. 4 (f). (iv) polynomial fitting tool with 7th order was used to fit the contour of the molten pool (Fig. 4 (g)), which was further overlayed on the raw image (Fig. 4 (h)).

3.2. Determining the curvature of molten pool boundary

The curvature function was employed as a quantitative tool to identify the morphological characteristics of the molten pool under different process parameters. The curvature (K) at each point along the contour of molten pool indicates the extent of localised bending of the molten pool boundary and can be expressed by the Eq. (5),

$$K = \frac{X''.Y' - Y''.X'}{(X')^2 + (Y')^2} \tag{5}$$

where X'', Y'', X', and Y' are the second and first derivate of the molten pool contour coordinates obtained from the algorithm.

3.3. Crystallization paths of growing dendrites

Fig. 5 (a) schematically illustrates the assumption that the preferred grain growth aligns with the normal to the molten pool shape. The alignment approximates the higher thermal gradient direction, indicating the favoured crystallisation path of dendrites [30]. Furthermore, crystallisation paths of the growing dendrites were predicted using the Euclidean distance approach [37], with the normal molten pool minimising the distance between consecutive molten pools across time frames. The minimal distance from a given point to the curve B (X, Y) of the molten pool contour can be characterised as the perpendicular line extending from the point to the curve. The initial point $P_1(x_o, y_o)$ is determined from the onset of the molten pool as illustrated in Fig. 5 (a). Subsequently, the minimal distance was measured to find the closest point between the boundary B and point P_1. The point on B closest to P_1 is then designated as the point P_2, marking the next position in the crystallisation path. The boundary coordinates were represented by X = x_1, x_2, x_3, …, x_n; Y = y_1, y_2, y_3, …, y_n, and the minimal distance was measured using the Euclidean distance,

$$P_2(x_j, y_j) = \min\left(\sqrt{(x_i - x_o)^2 + (y_i - y_o)^2}\right), \text{ for } i = 1 \text{ to } n, j = 1 \text{ to } m \tag{6}$$

where n is the number of points on the molten pool boundary, and m is the number of points on the trajectory. Note that these crystallisation paths, derived from estimating grain boundaries from the molten pool shape, potentially indicate the early onset of crack initiation as shown in the optical micrograph in Fig. 5 (b). Further, it can be correlated to the shrinkage and thermal contraction stresses induced during cracking near these paths.

4. Results and discussions

This study presents a novel approach to observe the through thickness molten pool shape using high speed camera investigations from the melt-glass experiment, elucidating its role in cracking susceptibility. Fig. 6 shows the through-thickness molten pool shape determined from the developed algorithm and compares with the results generated from the available models in literature which are previously used for monitoring the top surface molten pool shape using edge-detecting techniques [14] and frame subtraction methodologies [13]. The performance of these different models was evaluated using the ratio of the predicted area from the model that overlapped with the direct measurement of the evolving molten pool. Overall, the proposed approach in this study exhibits an accuracy of 94.3 %, while the model developed by Zhang Y et al., [14] and by Caprio L et al. [13] show an accuracy of 30.23 % and 42.5 %, respectively. Although [14] and [13] and are effective in detecting the top surface molten pool, they are inaccurate in capturing the highly dynamic and complex texture of the through-thickness molten pool shape. The model developed by Zhang Y et al., [14] using a Gaussian-Laplacian edge detector and image processing techniques, failed to segment the molten pool shape due to the presence of complex texture, the significant influence of noise and low contrast within the welding conditions, as depicted in Fig. 6 (a). Similarly, the molten pool shape generated from the model by Caprio L et al. [13] showed weak correlation with the actual shape of molten pool as it relied on frame subtraction with logarithmic differences and used a combination of filtering and image processing techniques, leading to less accurate detection of the dynamic background and illumination coupled with occlusions in the image as shown in Fig. 6 (b). Addressing these limitations, the proposed approach in Fig. 6 (c) incorporated the optical flow method in conjunction with the image morphological operations. The coarse to fine LK method of optical flow provides detailed motion analysis and is robust to illumination changes in the image [38]. Furthermore, it accurately estimates and distinguishes the faculae of spattering, plasma and the complex texture on the through-thickness molten pool shape.
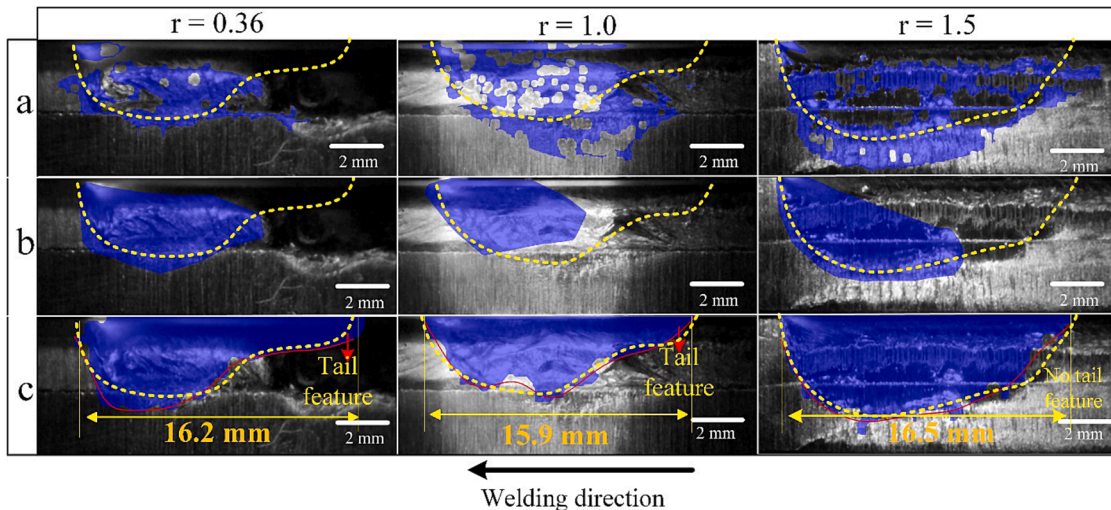

Fig. 6. Comparison of the of the prior research models that has been applied for welding (a) Zhang et al [14] model, (b) Caprio L et al [13] model, and (c) developed algorithm model of the molten pool shape at varying process parameters of laser power of 4000 W and power ratio of 0.36, 1.0 and 1.5.

Nevertheless, the developed methodology has a few limitations which might compromise its robustness in evaluating the molten liquid flow. Firstly, when the field of view is obstructed by the molten liquid metal which gets deposited and causes cloudiness on the quartz glass setup. Secondly, the experimental setup necessitated image cropping to avoid the plasma and the secondary melting at the bottom region. The secondary melting is attributed to the refractive nature of the quartz glass used in this setup which refracts the laser and melts the bottom region of the sample. Moreover, the spatial resolution of the imaging is another limitation in detecting the fluid flow when porosities and defects develop during the welding process. However, this model reduces the faculae present within the images resulting from the molten pool spattering and illumination, providing an accurate estimate of the molten pool shape amidst the complex texture observed in welding conditions, as compared to the models depicted in Fig. 6 (a), and (b).

Fig. 6 (c) depicts the through-thickness molten pool predicted by the developed algorithm at three different power ratios while maintaining a consistent total power of the ARM beam. It should be noted that from our prior numerical and in-situ monitoring investigations, a consistent tear drop shape near the top surface of the molten pool was identified, irrespective of varying power ratios, provided the total power remained constant [27,39]. These observations were further confirmed in the current study as the molten pool length remained consistent for the varying power ratio. However, a tail-like feature of the molten pool was identified for the first time, to the author's knowledge, through in-situ experimental observation, and this feature was less obvious as the power ratio increases. Interestingly, this observation aligns with various simulation studies of the through-thickness molten pool shape which proposed that the tail-like feature is associated with an extended solidification process and could eventually increases the crack sensitivity [9,40].

Therefore, the curvature of the molten pool boundary determined from the proposed model was utilised to quantify the evolution of this tail-like feature, as shown in Fig. 7. In this context, the curvature (K) derived in our methodology, reflects the local bending in the molten pool boundary. A higher K value, as observed in Fig. 7 (a), indicates a greater degree of bending in shape, characterising it to a notable tail-like feature. This is also accompanied by a noticeable shift in the centroid (SC) of the curvature plot towards the rear end.

$$SC = (\text{Center of the curvature plot}$$
$$- \text{Centroid of the curvature plot at that frame}) \tag{7}$$

This shift of centroid quantifies the degree of tail-like feature in the molten pool. Specifically, the further the centroid moves towards the

rear with SC as negative, the more pronounced the tail-like feature becomes.

In contrast, a more homogeneous molten pool was characterised by a uniform curvature along the molten pool boundary and the deviation of the centroid into the centre or front side of the molten pool, as depicted in Fig. 7 (b) and (c). Therefore, the observation of a shift in the centroid to the rear end of the curvature plot indicates a tail-like feature. This feature of the molten pool may effectively prolong the solidification leading to the increased and thermal contraction stresses during welding in the through-thickness direction. Furthermore, the presence of tail-like feature in the molten pool could be attributed as a result of the interplay between Marangoni convection stresses and the material flow due to the recoil pressure [9]. The dominated Marangoni forces in the upper region of the molten pool with the recirculation flow and the recoil pressure from the lower region of the molten pool convergingly induces a back-flow [40]. The cumulative effect of both these dominant forces creates a recirculation flow consequently results in the observed molten pool shape variations at the trailing end [41]. Moreover, in ref [9,41], a significant influence on the solidification behaviour was postulated with an extended molten pool as it causes a very short local weld pool lifetime at the bottom region and leads to early solidification when compared to top region of the fusion zone. Further, it leads to development of local tensile stresses during solidification that cannot be balanced by the molten liquid leading to a crack.

Fig. 8 shows the dynamic analysis of the through-thickness molten pool characteristics while predicting the trend of these variables using a sixth degree polynomial fit. It is observed that the molten pool length remains relatively consistent across varying power ratios during the welding. This indicates the significance of investigating the through-thickness molten pool shape, as the effects of beam shape with Adjustable Ring Mode (ARM) cannot be discerned solely from the top view observation during the welding process. Notably for the penetration depth, it is found that a lower and more stable penetration depth is achieved at the power ratio of 0.36. However, as the power ratio increases to 1.0, the stability of the penetration depth diminishes, suggesting and increasing stability of the laser keyhole welding when a higher ring power in ARM beam configurations utilised [42]. Following this, the shift in centroid of the curvature curve (K) as derived in Equation (7), is calculated for each frame of the through-thickness molten pool shape. As discussed, this shift denoted as SC (Shift in centroid of Curvature curve), is indicative of the overall bending of the molten pool boundary. The higher the SC (Shift in Centroid of Curvature) as shown in Fig. 8 (a), the higher the bend and as well as the higher tail-like feature in the molten pool shape are expected. Comparing SC values across Fig. 8 (a) –(c) it is evident that the bending of the curvature
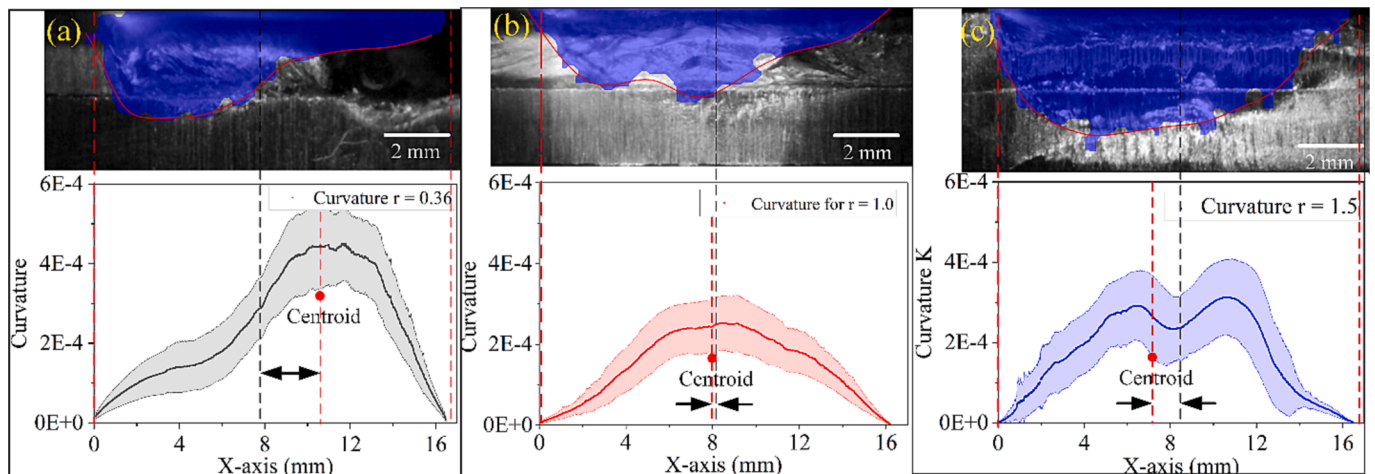

Fig. 7. Graphical representation of curvature variations over time for different molten pool shape observations, depicting the bends observed to identify the tail-like feature at power ratios of (a) r = 0.36, (b) r = 1.0, and (c) r = 1.5.
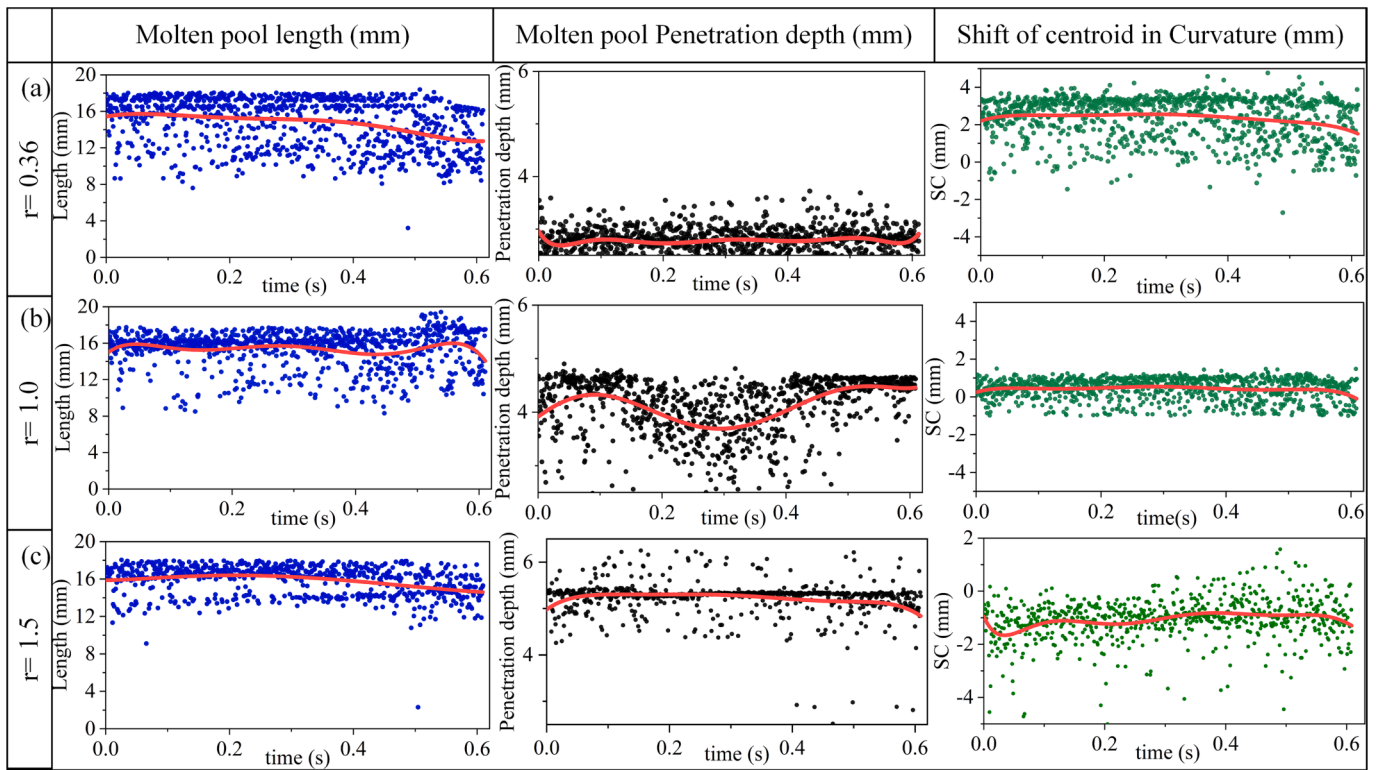
Fig. 8. Dynamic analysis with a 6th degree polynomial fit illustrating variations in through-thickness molten pool characteristics such as length, penetration depth and centroid shift, across three different power ratios (a) r = 0.36, (b) r = 1.0 and (c) r = 1.5.

of the molten pool transition from positive (towards the rear) to negative (towards the front) as the power ratio is increased. This is the due to the reduced tail-like feature in the molten pool boundary at power ratio of 1.5 that decreases the degree of bend in the curvature and the SC shifts towards the front end reaching a mean value of −1 mm. Further, the need for observing and quantifying the tail-like feature in the molten pool will be discussed using the probable grain paths from the extracted molten pool shape.

Fig. 9 (a)-(c) illustrates the crystallisation paths within the corresponding molten pool shapes as predicted by the proposed model considering the mean molten pool morphology from the dynamic analysis. It is important to note that significant amount of equiaxed grains formed near the top surface of the weld due to the rapid cooling process and resultantly the high nucleation rate [30]. Additionally, the columnar grains nucleate from the bottom of the molten pool perpendicular to the solid–liquid interface [30,43] and grow along the higher thermal gradient direction across the molten pool shape, leading to growth in length of columnar grains [44]. The modelled crystallisation paths or grain growth paths provides an estimation of growth direction of these columnar grains, leveraging on the principle of directional solidification which typically occurs along the steeper thermal gradient direction normal to the through-thickness molten pool shape [7,30]. Notably, the tail-like feature in the molten pool significantly affects the growth orientation of dendrites. In Fig. 9 (a) with a power ratio of 0.36, the estimated crystallisation paths predominantly exhibit a near-vertical paths due to the acute angle change in the rear end of molten pool shape as it moves along the welding direction. These grain growth paths align with the higher thermal gradient direction, influenced by the extended tail-like feature. The grain growth in the vertical direction paths leads to a higher susceptibility to the shrinkage-induced strains owing to this relatively vertical propagation of the grain boundaries during solidification. It potentially amplifies the strain concentration and promotes crack propagation along these paths [43]. Furthermore, as the power ratio increases, from Fig. 9 (b) and (c), a notable inclination of the

crystallisation paths is observed, which is associated with the expansion of the molten pool shape in the depth direction. The diminished tail-like feature at the rear end of the molten pool increases the tendency to form inclined paths due to the continuous and uniform decrease in the molten pool shape at the rear boundary. The change in paths inclination, particularly at the grain boundaries, may generate a breakage in the dendritic grain structure due to vigorous molten metal movement, resultantly facilitating more equiaxed grains in the fusion zone [45].

Furthermore, as illustrated in Fig. 9 (a), the presence of a tail-like featured molten pool shape indicates rapid solidification at the bottom region. This premature solidification leads to the development of local tensile strains, that cannot be balanced by the less remaining inter-dendritic liquid metal [9]. Fig. 9 (d) depicts the strain concentration levels along the estimated vertical grain growth paths. According to Prokhorov [46], cracks are likely to form when the deformation generated by the shrinkage and thermal contraction strains exceeds the resilience of the inter-dendritic film. Additionally, linear and elongated grains boundaries are more prone to this phenomenon as they are less capable of withstanding strains compared to isotropic, randomised equiaxed grains which distribute these strains more evenly across the solidified region [48]. Similar studies have proved that the direction of steep thermal gradients is the source of thermal strains in the welded region [47,48]. As depicted in Fig. 9 (d), a notable peak strain level of $\varepsilon_{xy} \cong 0.045$ was evident, suggesting an elevated probability of crack sensitivity along these predicted grain growth paths according to authors' previous study [25] where more vertical and elongated columnar grains were determined in welds at a lower power ratio, corresponding to a higher thermal strain and more frequent presence of centreline cracks. As the power ratio increases and the SC shifts towards the front end of the molten pool, the grain concentration is estimated to increase due to the inclined grain growth paths, which facilitates the distribution of strains across a broader area of grain boundaries. This distribution is further evidenced in Fig. 9 (e) and (f), where a decrease in strain levels with peak of $\varepsilon_{xy} < 0.01$ is depicted, suggesting a reduced cracking
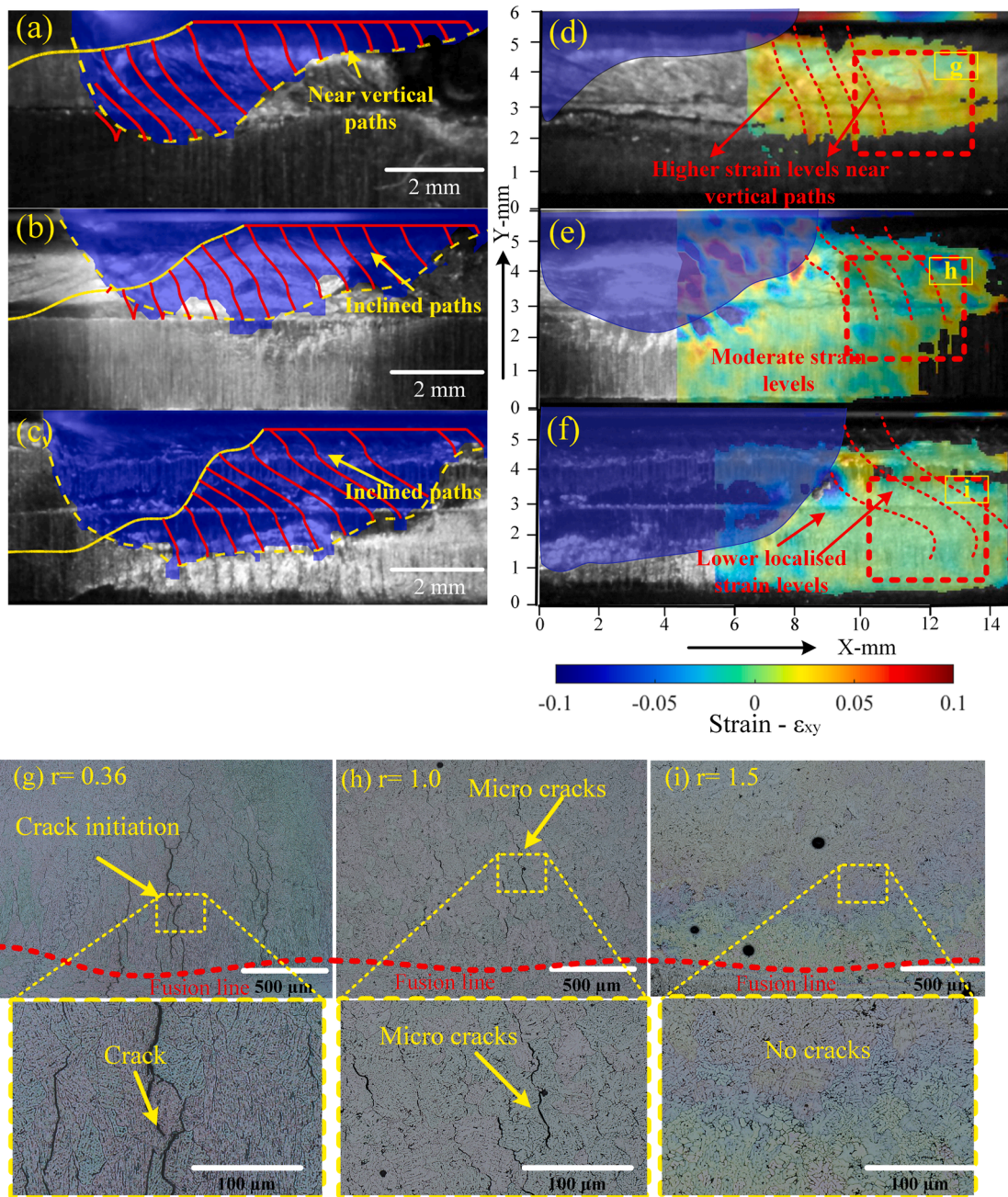
Fig. 9. Contour maps illustrating the path of growing dendrites at various molten pool shapes (a) r = 0.36, (b) r = 1.0, (c) r = 1.5 with the strain evolution of the through-thickness model using the DIC (Digital Image Correlation) for power ratio (d) r = 0.36, (e) r = 1.0, (f) r = 1.5 and the optical micrographs showing the crack propagation.

sensitivity.

Further, Fig. 10 shows the effect of increased inclination and the reduced tail-like features on the microstructural characteristics. The premature or early solidification at the bottom region is prominent at a lower power ratio (ring laser dominates) due to a higher thermal gradient [39] in the top region of the molten pool, where a higher Marangoni convection stresses results in extended tail-like feature and consequently leads to higher localised strains in both X and Y direction as depicted in Fig. 10 (a). Moreover, the EBSD micrographs in Fig. 10 (c), (d), (e) and (f), confirm the preferred growth direction of columnar grain in the ⟨1 0 0⟩ direction, indicating the propensity for columnar grains to align with the higher thermal gradient direction. This supports the explanation of increasing strain levels in the case of lower power ratio. As the power ratio increases where a deeper keyhole is observed, the

backward flow is enhanced due to greater recoil pressure, pushing more fluid towards the rear end and reducing the tail-like feature of the molten pool [49]. Consequently, it resulted in tensile contraction strains dominantly in X-direction as illustrated in Fig. 10 (b) and an increased number of grains in the fusion zone. While the exact underlying mechanism of the solidification crack propagation are not confirmed based on the molten pool shape, this study demonstrates the efficacy of the through-thickness molten pool shape for site specific crack sensitivity control.

Based on the discussion above, it can be understood that the SC of through-thickness molten pool boundary curvature deviating into the rear (positive) of molten pool indicates a significant tail-like feature which is associated with strain acting along the vertical crystallisation trajectory of the growing dendrites. It hypothetically indicates
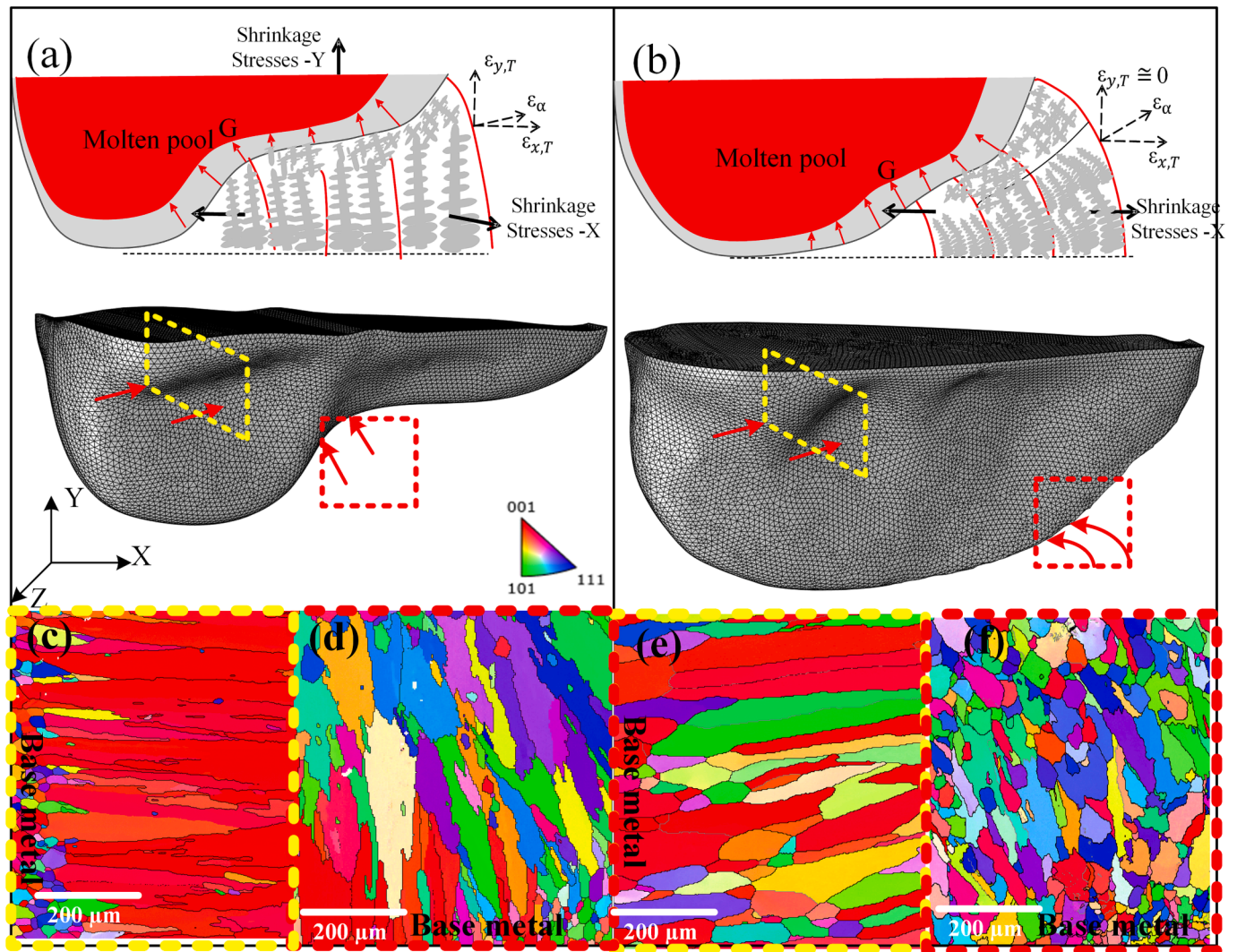
Fig. 10. Schematic of the shrinkage and thermal contractions strains acting along with reconstructed molten pool geometry from the estimated molten pool and the EBSD micrographs for (a) tail-like feature molten pool shape, and (b) expanded molten pool shape.

premature solidification and increased strains with higher crack sensitivity due to a tail-like feature in the molten pool. Conversely, a uniform curvature with the centroid near the centre or the front-end of the boundary curvature signifies low strain levels in the fusion zone. Future investigations and numerical simulations are required to identify the molten pool behaviour at different beam shapes and the influence of tail-like feature. Nevertheless, the results from the present investigation show that monitoring the through-thickness molten pool shape can be potentially employed as an indirect indicator of crack sensitivity.

5. Summary

In the current study, a robust methodology for the estimation of through-thickness molten pool shape and its effect on crack susceptibility in ARM laser welding has been studied by in-situ monitoring with high-speed camera in aluminium-glass butt welding experiments. Further, an image processing algorithm and a curvature analysis have been developed to extract the salient features of the molten pool shape and its effect on crack sensitivity.

- The proposed image processing algorithm addressed the limitations from the advanced models available in the literature and offers detailed motion analysis and segments of the through-thickness molten pool shape with an improved accuracy of 94.3 %.

- A tail-like feature was identified at the rear end of the through-thickness molten pool using the developed algorithm. As the power ratio increased from 0.36 to 1.5, the tail-like feature is diminished, leading to a more uniform the molten pool shape.

- The early solidification with a near vertical estimated crystallisation paths for a tail-like feature molten pool shape leads to the reduced lifetime of the molten metal at the bottom region. This facilitates the development of local tensile strains during solidification as determined from the DIC strains. For the uniform through-thickness molten pool shape with a power ratio of 1.5, the inclination in crystallisation paths increases the grain concentration and mitigates the shrinkage strains acting along the depth direction.

CRediT authorship contribution statement

Venkat Vivek Pamarthi: Conceptualization, Data curation, Formal

analysis, Investigation, Methodology, Validation, Visualization, Writing – original draft, Writing – review & editing. **Tianzhu Sun:** Investigation, Methodology, Project administration, Software, Supervision, Writing – review & editing. **Abhishek Das:** Project administration, Supervision, Writing – review & editing. **Pasquale Franciosa:** Conceptualization, Methodology, Project administration, Resources, Software, Supervision, Writing – review & editing.

Declaration of competing interest

The authors declare that they have no known competing financial interests or personal relationships that could have appeared to influence the work reported in this paper.

Data availability

Data will be made available on request.

References

[1] T. Sun, P. Franciosa, C. Liu, F. Pierro, D. Ceglarek, Effect of micro solidification crack on mechanical performance of remote laser welded AA6063-T6 fillet lap joint in automotive battery tray construction, Appl. Sci. 11 (2021) 4522, https://doi.org/10.3390/app11104522.

[2] T. Sun, P. Franciosa, M. Sokolov, D. Ceglarek, Challenges and opportunities in laser welding of 6xxx high strength aluminium extrusions in automotive battery tray construction, Procedia CIRP 94 (2020) 565–570, https://doi.org/10.1016/j.procir.2020.09.076.

[3] J.C. Lippold, Solidification Behavior and Cracking Susceptibility of Pulsed-Laser Welds in Austenitic Stainless Steels A shift in solidification behavior under rapid solidification conditions promotes an increase in cracking susceptibility, Weld. J. (Miami); (United States) (1994) 73:6. https://www.osti.gov/biblio/7167543.

[4] S. Kou, Solidification and liquation cracking issues in welding, JOM 55 (2003) 37–42, https://doi.org/10.1007/s11837-003-0137-4.

[5] S. Geng, P. Jiang, X. Shao, G. Mi, H. Wu, Y. Ai, C. Wang, C. Han, R. Chen, W. Liu, Y. Zhang, Effects of back-diffusion on solidification cracking susceptibility of Al-Mg alloys during welding: A phase-field study, Acta Mater. 160 (2018) 85–96, https://doi.org/10.1016/j.actamat.2018.08.057.

[6] M. Bayat, A. Thanki, S. Mohanty, A. Witvrouw, S. Yang, J. Thorborg, N.S. Tiedje, J. H. Hattel, Keyhole-induced porosities in Laser-based Powder Bed Fusion (L-PBF) of Ti6Al4V: High-fidelity modelling and experimental validation, Addit. Manuf. 30 (2019) 100835, https://doi.org/10.1016/j.addma.2019.100835.

[7] S. Kou, Solidification cracking susceptibility associated with a teardrop-shaped weld pool, Sci. Technol. Weld. Join. (2021), https://doi.org/10.1080/13621718.2021.1910179.

[8] G. Agarwal, A. Kumar, I.M. Richardson, M.J.M. Hermans, Evaluation of solidification cracking susceptibility during laser welding in advanced high strength automotive steels, Mater. Des. 183 (2019), https://doi.org/10.1016/j.matdes.2019.108104.

[9] M. Bachmann, X. Meng, A. Artinov, M. Rethmeier, Evaluation of narrowed weld pool shapes and their effect on resulting potential defects during deep penetration laser beam welding, J. Laser Appl. 34 (2022) 042005, https://doi.org/10.2351/7.0000733.

[10] T. Nagira, D. Yamashita, M. Kamai, H. Liu, Y. Aoki, K. Uesugi, A. Takeuchi, H. Fujii, In situ observation of solidification crack propagation for type 310S and 316L stainless steels during TIG welding using synchrotron X-ray imaging, J. Mater. Sci. 56 (2021) 10653–10663, https://doi.org/10.1007/s10853-021-05969-0.

[11] K. Schwarzkopf, R. Rothfelder, M. Rasch, M. Schmidt, Two-color-thermography for temperature determination in laser beam welding of low-melting materials, Sensors 23 (2023), https://doi.org/10.3390/s23104908.

[12] F. Dorsch, H. Braun, S. Keßler, D. Pfitzner, V. Rominger, NIR-camera-based online diagnostics of laser beam welding processes, High Power Laser Mater. Process.: Lasers Beam Deliv. Diagnostics Appl. 8239 (2012) 82390T, https://doi.org/10.1117/12.908646.

[13] L. Caprio, A.G. Demir, B. Previtali, Observing molten pool surface oscillations during keyhole processing in laser powder bed fusion as a novel method to estimate the penetration depth, Addit. Manuf. 36 (2020), https://doi.org/10.1016/j.addma.2020.101470.

[14] Y. Zhang, X. Gao, Analysis of characteristics of molten pool using cast shadow during high-power disk laser welding, Int. J. Adv. Manuf. Technol. 70 (2014) 1979–1988, https://doi.org/10.1007/s00170-013-5442-7.

[15] L.J. Zhang, G.F. Zhang, X.Y. Bai, J. Ning, X.J. Zhang, Effect of the process parameters on the three-dimensional shape of molten pool during full-penetration laser welding process, Int. J. Adv. Manuf. Technol. 86 (2016) 1273–1286, https://doi.org/10.1007/s00170-015-8249-x.

[16] D. You, X. Gao, S. Katayama, A novel stability quantification for disk laser welding by using frequency correlation coefficient between multiple-optics signals, IEEE/ASME Trans. Mechatron. 20 (2015) 327–337, https://doi.org/10.1109/TMECH.2014.2311097.

[17] W. Huang, X. Gao, Y. Huang, Y. Zhang, Improved convolutional neural network for laser welding defect prediction, Int. J. Precis. Eng. Manuf. 24 (2023) 33–41, https://doi.org/10.1007/s12541-022-00729-9.

[18] T. Nagira, D. Yamashita, M. Kamai, H. Liu, Y. Aoki, H. Fujii, K. Uesugi, A. Takeuchi, Time-resolved X-ray imaging of solidification cracking for Al-Cu alloy at the weld crater, Mater. Charact. 167 (2020) 110469, https://doi.org/10.1016/j.matchar.2020.110469.

[19] N. Kouraytem, P.J. Chiang, R. Jiang, C. Kantzos, J. Pauza, R. Cunningham, Z. Wu, G. Tang, N. Parab, C. Zhao, K. Fezzaa, T. Sun, A.D. Rollett, Solidification crack propagation and morphology dependence on processing parameters in AA6061 from ultra-high-speed x-ray visualization, Addit. Manuf. 42 (2021) 101959, https://doi.org/10.1016/j.addma.2021.101959.

[20] A. Artinov, M. Bachmann, X. Meng, V. Karkhin, M. Rethmeier, On the relationship between the bulge effect and the hot cracking formation during deep penetration laser beam welding, Procedia CIRP 94 (2020) 5–10, https://doi.org/10.1016/j.procir.2020.09.002.

[21] Y. Huang, T.G. Fleming, S.J. Clark, S. Marussi, K. Fezzaa, J. Thiyagalingam, C.L. A. Leung, P.D. Lee, Keyhole fluctuation and pore formation mechanisms during laser powder bed fusion additive manufacturing, Nat. Commun. 13 (2022) 1–11, https://doi.org/10.1038/s41467-022-28694-x.

[22] A. Artinov, N. Bakir, M. Bachmann, A. Gumenyuk, M. Rethmeier, Weld pool shape observation in high power laser beam welding, Procedia CIRP 74 (2018) 683–686, https://doi.org/10.1016/j.procir.2018.08.043.

[23] M. Jiang, X. Chen, Y. Chen, W. Tao, Mitigation of porosity defects in fiber laser welding under low vacuum, J. Mater. Process. Technol. 276 (2020) 116385, https://doi.org/10.1016/j.jmatprotec.2019.116385.

[24] M. Jiang, X. Chen, Y. Chen, W. Tao, Increasing keyhole stability of fiber laser welding under reduced ambient pressure, J. Mater. Process. Technol. 268 (2019) 213–222, https://doi.org/10.1016/j.jmatprotec.2019.01.026.

[25] V.V. Pamarthi, T. Sun, A. Das, P. Franciosa, Tailoring the weld microstructure to prevent solidification cracking in remote laser welding of AA6005 aluminium alloys using adjustable ringmode beam, J. Mater. Res. Technol. 25 (2023) 7154–7168, https://doi.org/10.1016/j.jmrt.2023.07.154.

[26] P.W. Wang, R.F. Haglund, D.L. Kinser, M.H. Mendenhall, N.H. Tolk, R.A. Weeks, Luminescence induced by low energy electron deposition in suprasil® and spectrosil® glasses, J. Non Cryst. Solids 102 (1988) 288–294, https://doi.org/10.1016/0022-3093(88)90145-7.

[27] V.V. Pamarthi, T. Sun, A. Das, P. Franciosa, Strain-based investigation on solidification crack susceptibility of 6005 aluminium using adjustable ring mode (ARM) laser welding, Procedia CIRP 111 (2022) 425–430, https://doi.org/10.1016/j.procir.2022.08.180.

[28] J. Yang, K. Bhattacharya, Augmented Lagrangian digital image correlation, Exp. Mech. 59 (2019) 187–205, https://doi.org/10.1007/s11340-018-00457-0.

[29] C. Pan, D. Xue, Y. Xu, J.J. Wang, R.J. Wei, Evaluating the accuracy performance of Lucas-Kanade algorithm in the circumstance of PIV application, Sci. China Phys. Mech. Astron. 58 (2015), https://doi.org/10.1007/s11433-015-5719-y.

[30] S. Kou, Welding Metallurgy, Second ed, John Wiley & Sons, Inc., Hoboken, New Jersey, 2003. Doi: 10.1002/0471434027.

[31] T. Liu, L. Shen, Fluid flow and optical flow, J. Fluid Mech. 614 (2008) 253–291, https://doi.org/10.1017/S0022112008003273.

[32] L.P.N. Mendes, A.M.C. Ricardo, A.J.M. Bernardino, R.M.L. Ferreira, A comparative study of optical flow methods for fluid mechanics, Exp. Fluids 63 (2022) 1–26, https://doi.org/10.1007/s00348-021-03357-7.

[33] Z. Wang, X. Yang, Moving Target Detection and Tracking Based on Pyramid Lucas-Kanade Optical Flow, 2018 3rd IEEE International Conference on Image, Vision and Computing, ICIVC 2018 (2018) 66–69. Doi: 10.1109/ICIVC.2018.8492786.

[34] J.-Y. Bouguet, Pyramidal implementation of the lucas kanade feature tracker, Intel Corporation, Microprocessor Research Labs (2000) 1–9. https://www.semanticscholar.org/paper/Pyramidal-implementation-of-the-lucas-kanade-Bouguet/aa972b40c0f8e20b07e02d1fd320bc7ebadfdfc7#citing-papers.

[35] O.A.B. Mohmmed, M. Ovinis, F. Mohd Hashim, Comparative analysis of multi-resolution optical flow techniques for flow rate estimation, 2015 10th Asian Control Conference (ASCC) (2015) 1–5. Doi: 10.1109/ascc.2015.7360338.

[36] D. Deng, DBSCAN Clustering Algorithm Based on Density, Proceedings - 2020 7th International Forum on Electrical Engineering and Automation, IFEEA 2020 (2020) 949–953. Doi: 10.1109/IFEEA51475.2020.00199.

[37] A. Kromm, M. Thomas, T. Kannengiesser, J. Gibmeier, F. Vollert, Assessment of the solidification cracking susceptibility of welding consumables in the varestraint test by means of an extended evaluation methodology, Adv. Eng. Mater. 24 (2022) 1–9, https://doi.org/10.1002/adem.202101650.

[38] A. Kushwaha, A. Khare, O. Prakash, M. Khare, Dense optical flow based background subtraction technique for object segmentation in moving camera environment, IET Image Process 14 (2020) 3393–3404, https://doi.org/10.1049/iet-ipr.2019.0960.

[39] T. Sun, A. Mohan, C. Liu, P. Franciosa, D. Ceglarek, The impact of Adjustable-Ring-Mode (ARM) laser beam on the microstructure and mechanical performance in remote laser welding of high strength aluminium alloys, J. Mater. Res. Technol. 21 (2022) 2247–2261, https://doi.org/10.1016/j.jmrt.2022.10.055.

[40] A. Artinov, M. Bachmann, M. Rethmeier, International Journal of Heat and Mass Transfer Equivalent heat source approach in a 3D transient heat transfer simulation of full-penetration high power laser beam welding of thick metal plates, Int. J. Heat Mass Transf. 122 (2018) 1003–1013, https://doi.org/10.1016/j.ijheatmasstransfer.2018.02.058.

[41] N. Bakir, Ö. Üstündag, A. Gumenyuk, M. Rethmeier, Influence of the weld pool geometry on solidification cracking in partial penetration high power laser beam

welding, Procedia CIRP 111 (2022) 397–400, https://doi.org/10.1016/j.procir.2022.08.174.

[42] L. Wang, M. Yao, X. Gao, F. Kong, J. Tang, M. Jun Kim, Keyhole stability and surface quality during novel adjustable-ring mode laser (ARM) welding of aluminum alloy, Opt Laser Technol 161 (2023) 109202. Doi: 10.1016/j.optlastec.2023.109202.

[43] J. Liu, S. Kou, Crack susceptibility of binary aluminum alloys during solidification, Acta Mater. 110 (2016) 84–94, https://doi.org/10.1016/j.actamat.2016.03.030.

[44] Z. Yan, W. Liu, Z. Tang, X. Liu, N. Zhang, Z. Wang, H. Zhang, Effect of thermal characteristics on distortion in laser cladding of AISI 316L, J. Manuf. Process 44 (2019) 309–318, https://doi.org/10.1016/j.jmapro.2019.06.011.

[45] T. Yuan, Z. Luo, S. Kou, Grain refining of magnesium welds by arc oscillation, Acta Mater. 116 (2016) 166–176, https://doi.org/10.1016/j.actamat.2016.06.036.

[46] N.N. Prokhrov, Refinement in the hot tearing of cast Al-Cu alloy, Russ. Cast. Prod. 2 (1962) 172–175. https://www.scopus.com/inward/record.uri?eid=2-s2.0-0242565656&partnerID=40&md5=ede08593a4789447988cd4479a26e2be.

[47] A. Mohan, D. Ceglarek, P. Franciosa, M. Auinger, Numerical study of beam oscillation and its effect on the solidification parameters and grain morphology in remote laser welding of high-strength aluminium alloys, Sci Technol Weld Join 28 (2023) 362–371, https://doi.org/10.1080/13621718.2022.2163341.

[48] T. DebRoy, H.L. Wei, J.S. Zuback, T. Mukherjee, J.W. Elmer, J.O. Milewski, A.M. Beese, A. Wilson-Heid, A. De, W. Zhang, Additive manufacturing of metallic components – Process, structure and properties, Prog. Mater. Sci. 92 (2018) 112–224, https://doi.org/10.1016/j.pmatsci.2017.10.001.

[49] A. Artinov, X. Meng, M. Bachmann, M. Rethmeier, Numerical analysis of the partial penetration high power laser beam welding of thick sheets at high process speeds, Metals (Basel) 11 (2021) 1–16, https://doi.org/10.3390/met11081319.